A novel visible-light-driven In-based MOF/graphene oxide composite photocatalyst with enhanced photocatalytic activity toward the degradation of amoxicillin

Cao Yang [a], Xia You [a], Jianhua Cheng [a,b,*], Huade Zheng [b], Yuancai Chen [a]

[a] *Ministry of Education Key Laboratory of Pollution Control and Ecological Remediation for Industrial Agglomeration Area, College of Environment and Energy, South China University of Technology, Guangzhou 510006, China*
[b] *South China Institute of Collaborative Innovation, Dongguan 523808, China*

ARTICLE INFO

ABSTRACT

A novel MIL-68(In)-NH$_2$/graphene oxide (GrO) composite was prepared as a visible-light-driven photocatalyst for the degradation of amoxicillin (AMX). The MIL-68(In)-NH$_2$/GrO composite exhibited much higher photocatalytic activity than pure MIL-68(In)-NH$_2$. Using 0.6 g L^{-1} MIL-68(In)-NH$_2$/GrO and pH = 5, 93% degradation and 80% TOC removal toward AMX could be achieved after irradiation time of 120 and 210 min, respectively. The enhanced activity for MIL-68(In)-NH$_2$/GrO can be attributed to the modification by using GrO, which not only acted as electron transporters for suppressing the photogenerated carrier recombination, but also played as a sensitizer for enhancing visible light absorption. Further experiments revealed that the solution pH had a significant impact on the photodegradation of AMX. In addition, MIL-68(In)-NH$_2$/GrO possessed good reusability and stability. Finally, the enhanced photocatalytic mechanism over MIL-68(In)-NH$_2$/GrO was also proposed, and h$^+$ and $^{\bullet}$O$_2^-$ were further determined to be the main active species in the photocatalytic system.

© 2016 Elsevier B.V. All rights reserved.

1. Introduction

The presence of antibiotics in the environment has been reported as an emerging risk to the biotic environment. Recently, amoxicillin (AMX), a broad-spectrum and semisynthetic β-lactam antibiotic, was found to have the largest usage for both human and animal use in China, according to the Zhang et al.'s market survey [1]. Due to its high consumption and continuous discharge, AMX was frequently detected in environmental samples with the concentrations in the range of μg-ng L^{-1} [2–4]. Although AMX has low toxicity and usually exists in the aquatic environment at rather low concentration levels, the emergence of antibiotic resistant bacteria and genes are more pressing concerns [5]. Moreover, due to its biorefractory nature, AMX could not be effectively removed in the urban wastewater treatment plants (WWTP) through the conventional wastewater treatment processes [6,7], and even the WWTP may promote the propagation and spread of resistant organisms [5,8,9]. Therefore, it is highly demanded to develop new alternative methods to address the water contamination problems.

In recent years, advanced oxidation processes (AOPs), such as Fenton, photo-Fenton, ozonation and semiconductor photocatalysis, have been proved to be new alternatives to the conventional processes on AMX removal [10–14]. Especially, in view of worldwide energy crisis, photocatalysis is recognized as the most promising solution for converting photo energy to chemical energy in a sustainable manner. And photocatalysis has been demonstrated to be highly efficient in degrading AMX into biodegradable compounds as well as CO$_2$, H$_2$O and inorganic ions [15,16]. However, it should be note that a complete removal of AMX achieved in several studies required a long time ($\geq$240 min) and even followed a low mineralization ratio ($\leq$40%) [17–20]. Therefore, new superior photocatalysts need to be explored to overcome these shortcomings.

Metal-organic frameworks (MOFs), a new class of porous crystalline materials, have attracted tremendous attention considering their broad application prospect. The pioneering work by Garcia et al. [21] proved that MOF-5 showed the semiconductor properties and photocatalytic activity. Since then, MOFs as photocatalysts have become a hot research topic in catalytic degradation of organic pollutants, CO$_2$ reduction and hydrogen evolution [22–24].

MIL-68(In)-NH$_2$, synthesized firstly by the Farrusseng's group [25], is constructed from infinite chains of InO$_4$(OH)$_2$ octahedra linked through the BDC-NH$_2$ ligands [26]. Very recently, Liang et al.'s study found that MIL-68(In)-NH$_2$ behaved as an efficient visible-light-driven semiconductor photocatalyst with excellent photoactivity for the reduction of Cr (VI) [27]. However, the photoactivity of MIL-68(In)-NH$_2$ could be restricted by its fast charge recombination. An opportunity to promote the photocatalytic performance of MIL-68(In)-NH$_2$ lies in an efficient strategy of compositing semiconductors with the electron acceptors. In this context, some composite photocatalysts, such as CdS-UiO-66(NH$_2$) [28], CQDs/Bi$_2$WO$_6$ [29] and TiO$_2$@MoS$_2$ [30], have been successfully synthesized and shown higher photocatalytic activity than the semiconductor matrixes. Graphene oxide (GrO), one of the most ideal candidates as electron acceptors, has received widespread research attention because of its unique optical property, conductivity and strong mechanical strength [31]. Currently, many studies have revealed that GrO could effectively enhance the photogenerated charge carrier separation owing to its superior visible light adsorptivity and electron transport ability, which led to an enhancement in photocatalytic performance [32–35]. More importantly, the introduction of GrO has been proven to effectively improve the structure stability of the materials [36] and inhibit the photocorrosion of the photocatalysts for better photostability [37,38]. Inspired by which, in this work we developed a novel MIL-68(In)-NH$_2$/GrO composite by a simple solvothermal method. To the best of our knowledge, this is the first time that the MIL-68(In)-NH$_2$/GrO composite was synthesized for visible-light-driven photocatalytic degradation of organic pollutants.

Herein, in this study we reported the solvothermal synthesis of the MIL-68(In)-NH$_2$/GrO composite. The structures, morphologies, optical and electronic properties and photocatalytic performance were investigated in detail. The photocatalytic activities of MIL-68(In)-NH$_2$/GrO on the photocatalytic degradation of AMX were evaluated sufficiently, including the effects of pH values, the stability of the photocatalyst and reactive specie trapping experiments. The photocatalytic mechanism induced by visible-light responsive MIL-68(In)-NH$_2$/GrO was also proposed to explain the photodegradation of AMX on it.

2. Experimental

2.1. Materials

Graphite powder, 2-aminoterephthalic acid and indium nitrate hydrate (In(NO$_3$)$_3$·xH$_2$O) were obtained from Alfa Aesar China Co., Ltd. (Tianjin, China). Sulfuric acid (H$_2$SO$_4$), hydrochloric acid (HCl), sodium hydroxide (NaOH), potassium permanganate (KMnO$_4$), hydrogen peroxide (H$_2$O$_2$), $N'N$-dimethylformamide (DMF) and methanol were supplied by Guangzhou Chemicals Co., Ltd. (Guangzhou, China). Benzoquinone (BQ), t-butanol and formate were purchased from Sinopharm Chemical Reagent Co., Ltd. (Shanghai, China). Monopotassium phosphate (KH$_2$PO$_4$) and orthophosphoric acid (H$_3$PO$_4$) (85% p.a.) were from Merck. All reagents were analytical grade and used as received. HPLC-grade acetonitrile and methanol (Merck) were used for HPLC analyses.

2.2. Synthesis of GrO, MIL-68(In)-NH$_2$ and MIL-68(In)-NH$_2$/GrO

GrO was prepared using the Hummers method as reported in reference [39]. The MIL-68(In)-NH$_2$ was prepared by a solvothermal method [27]. Typically, In(NO$_3$)$_3$·xH$_2$O (1.92 mmol) and BDC-NH$_2$ (0.645 mmol) were mixed with DMF (6.2 mL) until complete dissolution of the solids. Then, the mixture was transferred into the Teflon liner, sealed in a stainless steel autoclave and heated

at 125 °C for 5 h. After natural cooling, light yellow powder was collected, washed with DMF, and immersed in fresh methanol for three days. The methanol was changed once a day. Finally, samples were filtered and dried under vacuum at 100 °C for 12 h. The resulting sample was then kept in a desiccator.

The MIL-68(In)-NH$_2$/GrO composite was prepared by dispersing GrO powder (24.7 mg) in the well-dissolved indium nitrate/BDC-NH$_2$ mixture. The resulting suspension was subsequently stirred and subjected to the same synthesis procedure as that of MIL-68(In)-NH$_2$.

2.3. Characterizations

Powder X-ray diffraction (XRD) patterns were carried on a Bruker D8 Advance X-ray diffractometer operated at 40 kV and 40 mA with Cu Kα radiation. Raman spectra were measured on a Renishaw inVia Raman microscope with a laser excitation wavelength of 520 nm. Fourier transform infrared spectra (FTIR) were recorded on a Nicolet 5700 spectrometer with KBr pellets. Scanning electron microscope (SEM) was performed on a MERLIN Compact instrument. The Brunauer-Emmett-Teller (BET) surface area was measured at 77 K with a Micromeritics ASAP2020 instrument. Pore size distribution was analyzed by non-local density functional theory (NLDFT). X-ray photoelectron spectroscopy (XPS, Thermo ESCALAB 250XI) was employed to investigate the chemical composition of the samples. UV–vis diffuse reflectance spectra (DRS) were recorded on a UV-vis-NIR spectrophotometer (Varian Cary 500). The photoluminescence spectra (PL) were obtained using a fluorescence spectrometer (Hitachi F-7000). Both the electrochemical impedance spectra (EIS) and Mott-Schottky curves were measured on a Princeton electrochemical workstation (Princeton Applied Research PARSTAT 2273) using a three-electrode system. The total organic carbon (TOC) was measured on a TOC analyser (Elementar vario TOC). The zeta potentials were determined by dynamic light scattering analysis (Zeta sizer 3000HSA).

2.4. Evaluation of photocatalytic activity

In a typical experiment, the visible-light photocatalytic degradation of AMX was carried out at 23 ± 1 °C in a 500 mL jacketed glass reactor containing 120 mg photocatalyst and 200 mL of 20 ppm AMX aqueous solution. The solution pH was adjusted with HCl or NaOH. After being stirred in dark for 60 min to achieve adsorption-desorption equilibrium, the suspensions were irradiated by a 300 W Xe lamp (PLS-SXE 300, Beijing Perfectlight Co., Ltd) with a 420 nm cut-off filter. During illumination, sample aliquots were taken at pre-determined time intervals and filtered through 0.45 μm cellulose acetate syringe membrane filters for HPLC (Waters LC system) analysis, which comprised an XBridge column (4.6 × 250 mm, C18, 5 μm) and an UV–vis detector. Acetonitrile and 0.05 M KH$_2$PO$_4$ buffer solution acidified at pH 3 with H$_3$PO$_4$ were used as mobile phases A and B (v_A/v_B = 10/90), respectively, at a flow rate of 1 mL min^{-1}. The oven temperature was maintained at 25 °C. The detector wavelength was set at 230 nm and the injection volume was 10 μL.

3. Results and discussion

3.1. Characterizations

XRD patterns of GrO, MIL-68(In)-NH$_2$, their physical mixture GrO+MIL-68(In)-NH$_2$ and the MIL-68(In)-NH$_2$/GrO composite are shown in Fig. 1a. The diffraction pattern of the composite was nearly the same as that of the MIL-68(In)-NH$_2$ previously reported [26,27], suggesting that the crystalline characters of the parental MIL-68(In)-NH$_2$ were preserved in the composite. However, the
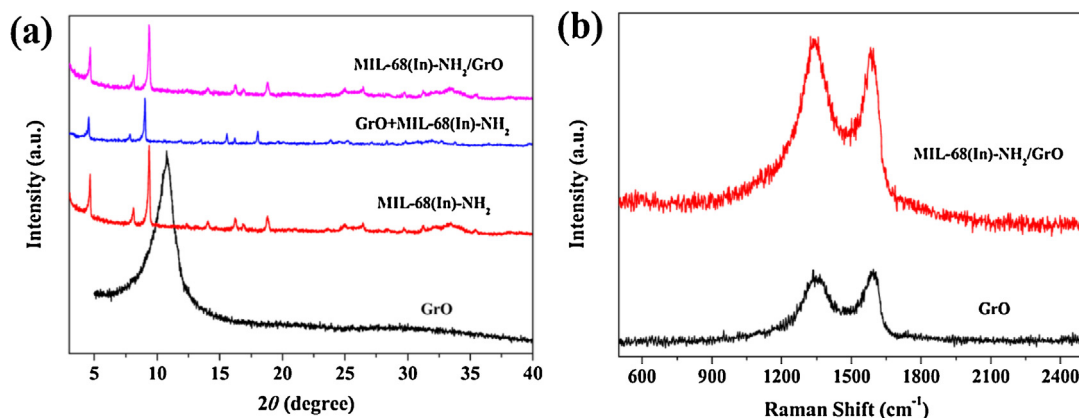
Fig. 1. (a) XRD patterns of GrO, MIL-68(In)-NH$_2$, GrO+MIL-68(In)-NH$_2$ and MIL-68(In)-NH$_2$/GrO. (b) Raman spectra of GrO and MIL-68(In)-NH$_2$/GrO.

typical diffraction peak of GrO was absent in the composite, which may be due to the low amount of GrO or the high dispersion of GrO in DMF [40]. Besides, it is noticed that the diffraction pattern of the composite MIL-68(In)-NH$_2$/GrO was different from that of the mixture GrO+MIL-68(In)-NH$_2$. The peak intensity of the mixture was significantly weaker than the MIL-68(In)-NH$_2$, which was possibly due to that the MIL-68(In)-NH$_2$ crystals in the mixture were partly sheltered by GrO [41]. And there was an obvious deviation in peak position when compared with the parental MIL-68(In)-NH$_2$ and the composite. The presence of GrO in the composite can be validated by Raman spectra. As shown in Fig. 1b, two obvious peaks are found to be located at 1350 and 1599 cm^{-1}, corresponding to the typical D and G bands, respectively [42]. Furthermore, a slight increased D/G intensity ratio (I_D/I_G = 1.04) for MIL-68(In)-NH$_2$/GrO was also obtained in comparison with that of GrO (I_D/I_G = 0.93), indicating that a fraction of GrO has been reduced during the solvothermal process.

Fig. 2a shows the FTIR spectra of GrO, MIL-68(In)-NH$_2$ and MIL-68(In)-NH$_2$/GrO. The FTIR spectrum of GrO showed the fingerprint groups, such as C=O stretching vibrations in carbonyl and carboxyl groups (1734 cm^{-1}), skeletal ring stretching (1627 cm^{-1}), OH deformation (1403 cm^{-1}), C—OH stretching vibrations (1228 cm^{-1}), epoxide C—O—C stretching vibration (1077 cm^{-1}) [43,44]. However, no obvious adsorption bands of GrO are found in MIL-68(In)-NH$_2$/GrO. Meanwhile, a significant decrease in the intensity ratio of the bands at 1621/1557 cm^{-1} for MIL-68(In)-NH$_2$/GrO is observed in comparison with pure MIL-68(In)-NH$_2$. And that must be connected with the interaction of the MOF and GrO. A similar result was also reported by Petit et al. [40]. In addition, as seen in Fig. 2b, the two bands at 3509 and 3395 cm^{-1} in the spectrum of MIL-68(In)-NH$_2$, which are attributed to the symmetric and asymmetric stretching vibrations of primary amines, were missing in MIL-68(In)-NH$_2$/GrO. However, it is likely that the broad peak of the bridging —OH of the framework and water molecules overlapped the two weak peaks.

Fig. 3 shows the SEM images of GrO, MIL-68(In)-NH$_2$ and MIL-68(In)-NH$_2$/GrO. It can be seen from Fig. 3a that the GrO showed a layered structure. Fig. 3b shows that the MIL-68(In)-NH$_2$ had needlelike morphology. For the MIL-68(In)-NH$_2$/GrO composite, it can be seen that the GrO and MIL-68(In)-NH$_2$ components were bonded together with GrO as an ideal support (Fig. 3c and d). Meanwhile, it is also observed that the sizes of the MIL-68(In)-NH$_2$ crystals in the MIL-68(In)-NH$_2$/GrO composite were significantly smaller than those of the parental ones. This indicates that the introduction of GrO in the composite had certain influences on the building of the MIL-68(In)-NH$_2$ crystals during the synthesis process. Furthermore, BET surface area measurements were conducted to examine the porous nature of the samples in our study.

Fig. 4a shows the N$_2$ isotherms of GrO, GrO+MIL-68(In)-NH$_2$, MIL-68(In)-NH$_2$ and MIL-68(In)-NH$_2$/GrO. GrO, as previously reported [45], can be considered as nonporous (Fig. S1). For GrO+MIL-68(In)-NH$_2$, MIL-68(In)-NH$_2$ and MIL-68(In)-NH$_2$/GrO, their isotherms all exhibited a type I isotherm in the IUPAC classification, demonstrating their microporous characteristics [46]. It is also noticed that the porosity of the GrO+MIL-68(In)-NH$_2$ mixture was obviously less than that of MIL-68(In)-NH$_2$/GrO. This may be ascribed to the partial coverage of MIL-68(In)-NH$_2$ by the GrO sheet, which led to the formation of a large number of mesopores and some macropores (Fig. S2). From the PSD analysis (Fig. 4a inset), it is observed that both MIL-68(In)-NH$_2$ and MIL-68(In)-NH$_2$/GrO contained two kinds of pore sizes of 5 and 16 Å, respectively. The calculated BET surface area is 681.0 m^2 g^{-1} for MIL-68(In)-NH$_2$/GrO, which is higher than that of the parental MIL-68(In)-NH$_2$ (530.4 m^2 g^{-1}). For the enhanced porosity on MIL-68(In)-NH$_2$/GrO, it may be closely related with the emerging mesopores created at the interface between the GrO and MIL-68(In)-NH$_2$ components, as evidenced by the observed hysteresis loop in the N$_2$ isotherm measured on MIL-68(In)-NH$_2$/GrO and the corresponding PSD plot.

Fig. 4b presents the high resolution In 3d XPS spectra of MIL-68(In)-NH$_2$ and MIL-68(In)-NH$_2$/GrO. It can be seen that there was a slight shift to higher binding energy in MIL-68(In)-NH$_2$/GrO compared to the pure MIL-68(In)-NH$_2$, which indicates a change in chemical binding of In. And this change may be attributed to the metal–GrO interactions on the MIL-68(In)-NH$_2$/GrO sample, which resulted in the covalent attachment of the MIL-68(In)-NH$_2$ to the GrO surfaces during the solvothermal reaction. In addition, such a shift in the positive direction also reflects a decrease in the electron density of In, suggesting that electron transfer occurred from the MIL-68(In)-NH$_2$ crystal to the GrO surface. The similar chemical shift in XPS was also reported by Samadi et al. [47] and Zhou et al. [48].

Besides the structural properties, the optical property of MIL-68(In)-NH$_2$ was also significantly affected by the GrO modification. As shown in Fig. 5, the bare GrO exhibited good light absorption performance in the range of 200–800 nm, which was also reported by Peng et al. [49]. MIL-68(In)-NH$_2$ showed slightly strong visible light absorption. After the incorporation of GrO, the remarkably enhanced visible light absorption occurred to the MIL-68(In)-NH$_2$/GrO composite. However, for the GrO+MIL-68(In)-NH$_2$ physical mixture, its light absorption ability was significantly weaker than that of MIL-68(In)-NH$_2$/GrO. In addition, it is important to note that a red shift of the absorption band edges of MIL-68(In)-NH$_2$/GrO vs. MIL-68(In)-NH$_2$ can be observed, meaning the bandgap narrowing of the MIL-68(In)-NH$_2$/GrO composite. Based on the Kubelka-Munk plots (Fig. 5 inset), the estimated bandgaps for MIL-68(In)-NH$_2$ and MIL-68(In)-NH$_2$/GrO are 2.62
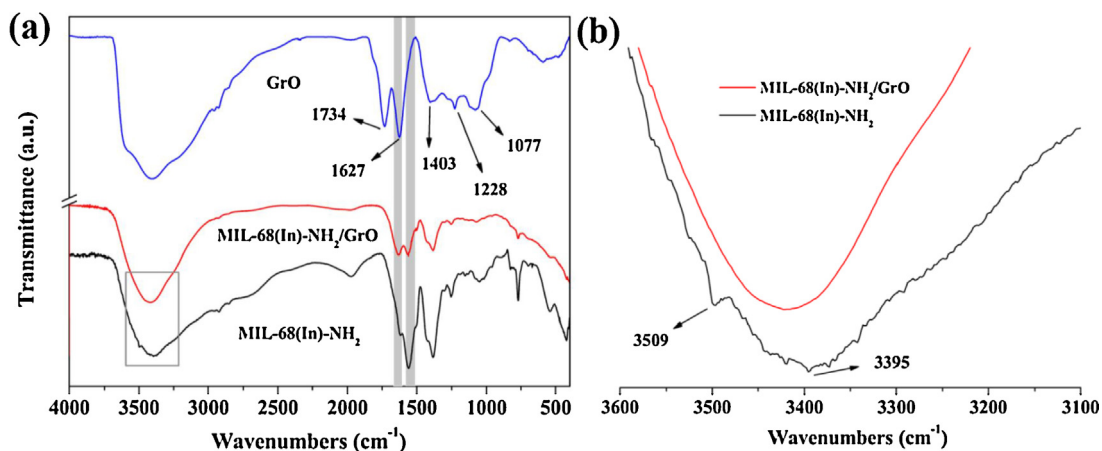
Fig. 2. FTIR spectra of (a) GrO, MIL-68(In)-NH$_2$ and MIL-68(In)-NH$_2$/GrO and (b) MIL-68(In)-NH$_2$ and MIL-68(In)-NH$_2$/GrO (3100–3600 cm^{-1}).
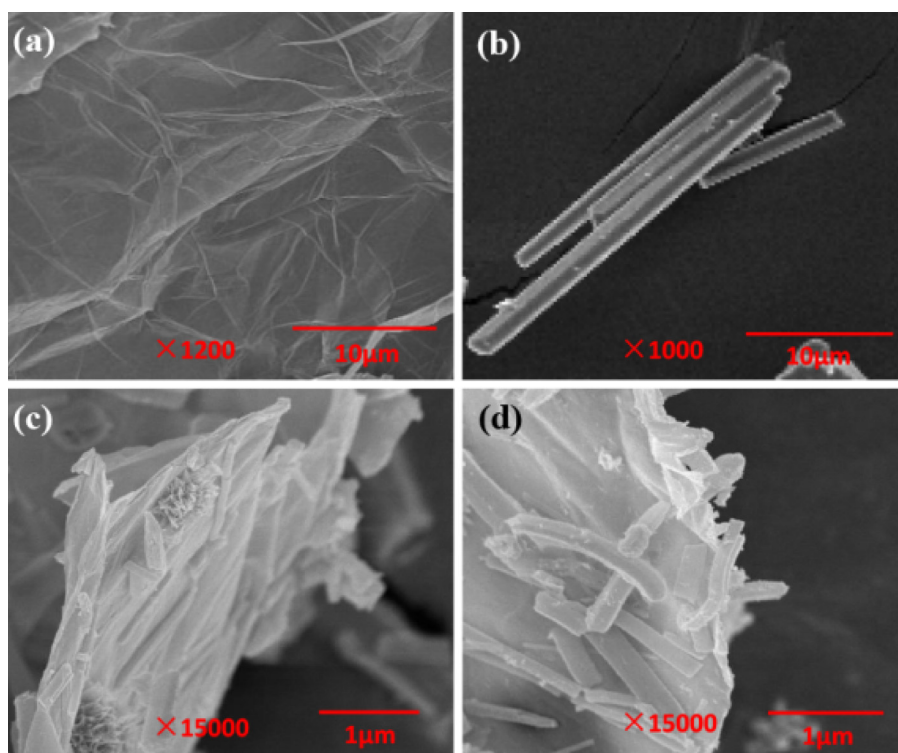

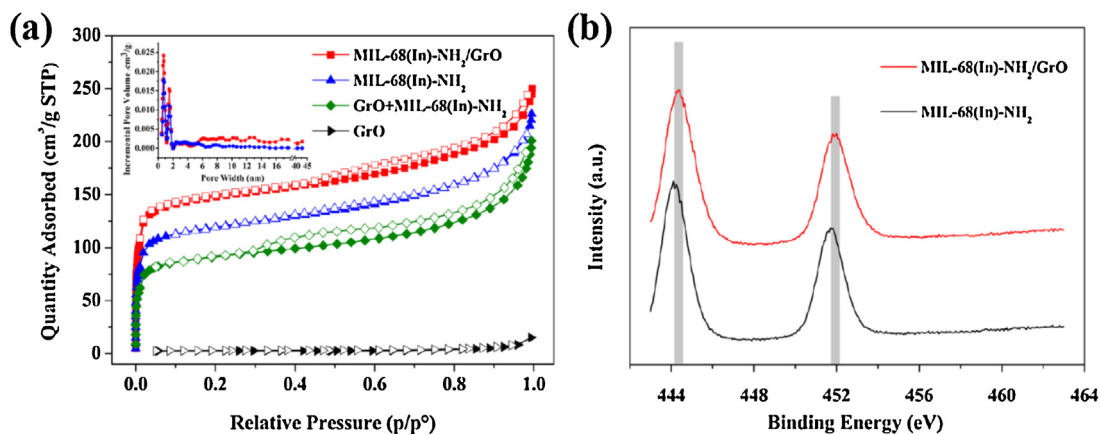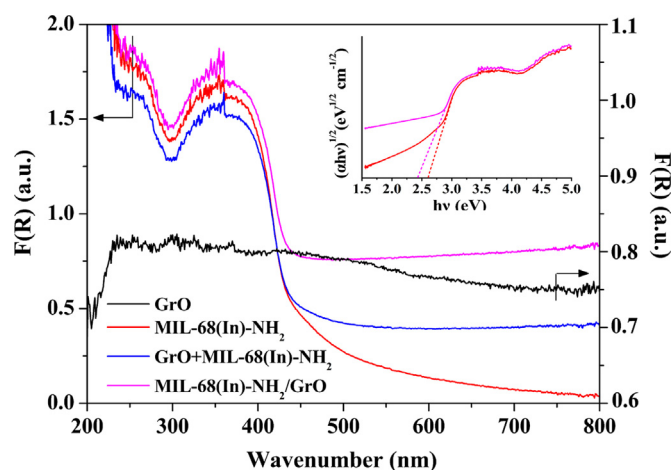**Fig. 3.** SEM images of (a) GrO, (b) MIL-68(In)-NH$_2$ and (c, d) MIL-68(In)-NH$_2$/GrO.

Fig. 4. (a) N$_2$ isotherms of GrO, GrO+MIL-68(In)-NH$_2$, MIL-68(In)-NH$_2$ and MIL-68(In)-NH$_2$/GrO. The inset shows the pore size distribution (PSD) plots of MIL-68(In)-NH$_2$ and MIL-68(In)-NH$_2$/GrO. (b) High resolution In 3d XPS spectra of MIL-68(In)-NH$_2$ and MIL-68(In)-NH$_2$/GrO.

Fig. 5. DRS of GrO, GrO+MIL-68(In)-NH$_2$, MIL-68(In)-NH$_2$ and MIL-68(In)-NH$_2$/GrO. The inset is the plots of transformed Kubelka-Munk function vs. the light energy of MIL-68(In)-NH$_2$ and MIL-68(In)-NH$_2$/GrO.

and 2.43 eV, respectively. In the case of MIL-68(In)-NH$_2$/GrO, noticeable enhancement of the absorptivity in visible-light region should be greatly connected with the introduction of GrO. Previous reports have proved that GrO played vital roles in enhancing the visible light harvesting capability of the semiconductors/GrO photocatalysts [50,51]. And the improved visible light absorption would be beneficial to the enhancement of photocatalytic activity of the MIL-68(In)-NH$_2$/GrO composite.

Photoluminescence (PL) analysis has been widely used to investigate the carrier separation efficiency of the photocatalysts. Fig. 6a presents the PL spectra of MIL-68(In)-NH$_2$ and MIL-68(In)-NH$_2$/GrO. The PL spectrum of the parental MIL-68(In)-NH$_2$ showed a strong emission peak at around 465 nm. Apparently, when GrO was introduced into the MOF framework, the intensity of this PL emission peak diminished significantly, which indicates a decreased recombination of photogenerated electron-hole pairs in MIL-68(In)-NH$_2$/GrO system. According to the PL analysis, it can be believed that the introduction of GrO efficiently enhanced the carrier separation efficiency and thus prolonged the carrier lifetime, which would benefit the improvement of the photocatalytic activity of MIL-68(In)-NH$_2$/GrO. To further validate this hypothesis, EIS measurements for MIL-68(In)-NH$_2$ and MIL-68(In)-NH$_2$/GrO were conducted to investigate the process of charge transfer and recombination. As is known to us, the diameter of the arc in the Nyquist plot is equal to the charge-transfer resistance (Rct) occurring at the semiconductor-electrolyte interface, and the smaller diameter of the Nyquist circle denotes the lower Rct. As seen in Fig. 6b, MIL-68(In)-NH$_2$/GrO showed a lower Rct compared to pure MIL-68(In)-NH$_2$, implying that a faster interfacial charge transfer to GrO as the electron acceptor occurred and led to the effective separation of photogenerated electrons and holes in MIL-68(In)-NH$_2$. The EIS result is in good agreement with the PL analysis, demonstrating that the introduction of GrO (electron acceptor) is an effective way to improve photocatalytic efficiency.
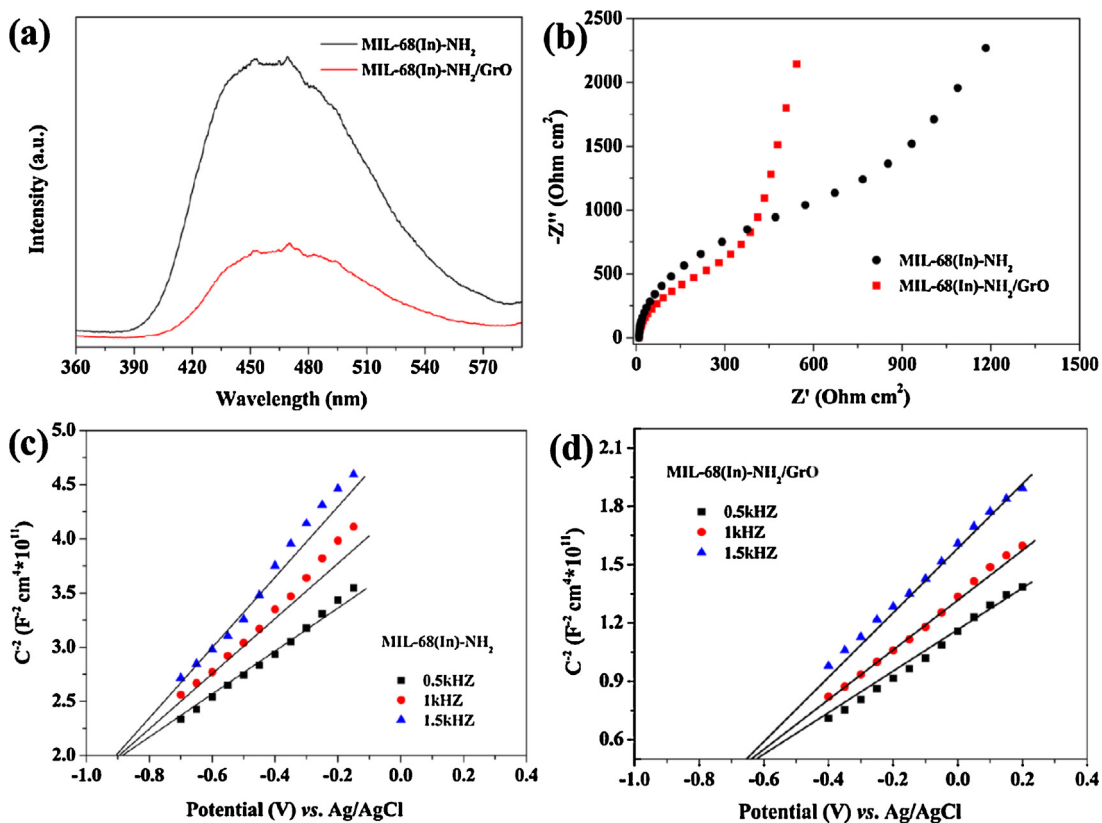
To further investigate the effect of the GrO modification on the band structure of the obtained materials, the flat-band potentials (E_{FB}) of MIL-68(In)-NH$_2$ and MIL-68(In)-NH$_2$/GrO were measured by performing the typical Mott-Schottky measurements. Fig. 6c and 6d respectively show the Mott-Schottky plots of MIL-68(In)-NH$_2$ and MIL-68(In)-NH$_2$/GrO, revealing their typical n-type semi-conductivity because of the positive slope [52,53]. For n-type semiconductors, their conduction band potential (E_{CB}) are very close to the E_{FB} [54]. Therefore, the E_{CB} deduced from Mott-Schottky plots are about −0.90 and −0.62 eV vs. Ag/AgCl (−0.68 and

−0.40 eV vs. NHE) for MIL-68(In)-NH$_2$ and MIL-68(In)-NH$_2$/GrO, respectively. Apparently, the conduction band edge potential of MIL-68(In)-NH$_2$/GrO showed a positive shift in comparison with MIL-68(In)-NH$_2$. Based on the bandgap values of MIL-68(In)-NH$_2$ and MIL-68(In)-NH$_2$/GrO obtained by DRS (Fig. 5 inset), the calculated valence band potentials (E_{VB}) are 1.94 and 2.03 eV vs. NHE, respectively. Compared to MIL-68(In)-NH$_2$, a positive shift also occurred to the E_{VB} of MIL-68(In)-NH$_2$/GrO. And this means that MIL-68(In)-NH$_2$/GrO would possess higher oxidation ability than pure MIL-68(In)-NH$_2$ in the photocatalytic process.
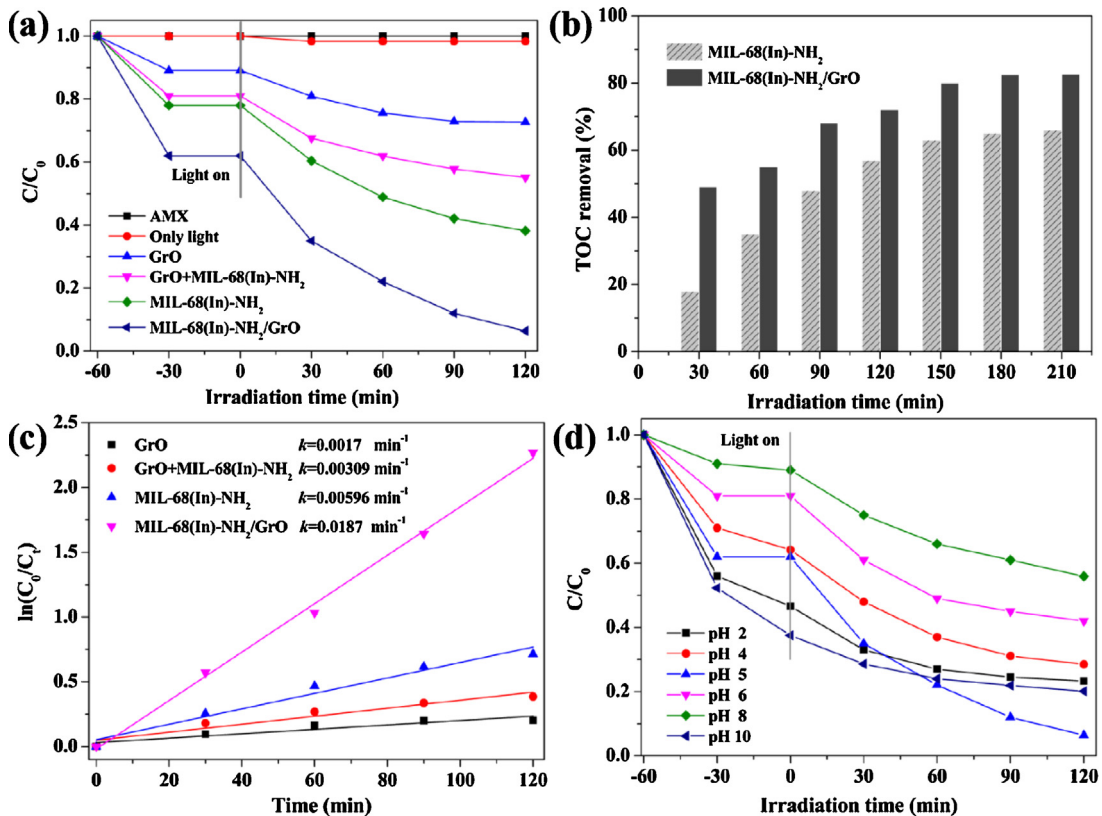
3.2. Photocatalytic activity and stability

AMX was stable toward hydrolysis at pH 5 [55]. Several control experiments were firstly performed to ensure that the results obtained from the photocatalytic tests were consistent and not affected by hydrolysis or photolysis. As shown in Fig. 7a, no significant decay in AMX concentration in the dark or during illumination was observed. Meanwhile, the blank experiment of GrO serving as a photocatalyst to degrade AMX was also carried out. The result showed that about 28% of AMX was removed, suggesting a certain photocatalytic activity of GrO for the degradation of AMX. While the presence of MIL-68(In)-NH$_2$ showed an increase in photocatalytic efficiency up to 60%. This was due to the characteristics of MIL-68(In)-NH$_2$, which could stimulate the visible light adsorption. However, a noticeable degradation of AMX was successfully achieved by the MIL-68(In)-NH$_2$/GrO composite; but for the GrO+MIL-68(In)-NH$_2$ mixture, its photocatalytic efficiency (45%) was far worse than that of the composite (93%). A similar behavior is also observed for the TOC removal. As shown in Fig. 7b, after irradiated by visible light for 210 min, more than 80% mineralization was obtained in the presence of MIL-68(In)-NH$_2$/GrO, which was higher than that of MIL-68(In)-NH$_2$ (~65%). It should be noted that the MIL-68(In)-NH$_2$/GrO composite possessed better photocatalytic and mineralization performance compared to the parental MIL-68(In)-NH$_2$. Also, it is found that the photocatalytic degradation of all the investigated photocatalysts toward AMX followed the pseudo-first-order kinetics model. Fig. 7c shows the kinetic fitting curves for the AMX degradation with different photocatalysts. The photocatalytic degradation rate of MIL-68(In)-NH$_2$/GrO toward AMX was almost 3.0 times of the pure MIL-68(In)-NH$_2$, 11.0 and 6.1 times of GrO and GrO+MIL-68(In)-NH$_2$, respectively. Obviously, the MIL-68(In)-NH$_2$/GrO composite displayed the best photocatalytic activity toward the degradation of AMX. All these results can prove effectively that the photocatalytic activity of MIL-68(In)-NH$_2$ can be enhanced through the modification of GrO.

Previous studies reported that the charged form of AMX is significantly affected by the pH of the reaction system and mainly exists in two forms: the positively charged ones at acid pH and negatively charged ones at alkaline pH [56,57]. Fig. 7d shows the photocatalytic degradation of AMX by MIL-68(In)-NH$_2$/GrO at different pH values. It can be seen that AMX could be quickly removed at pH 2 and 10. And it should be mainly due to the hydrolysis of AMX, confirmed by the blank experiments (Fig. S3), which easily occurred under strong acid and alkaline conditions [58,59]. Among all the investigated pH values, the best photocatalytic activity toward AMX degradation can be found at pH 5. In order to further explore the above phenomenon, the plot of zeta potential vs. pH for MIL-68(In)-NH$_2$/GrO is presented in Fig. S4. The zero point of charge (pH$_{zpc}$) of MIL-68(In)-NH$_2$/GrO was determined to be 4.13. Therefore, when the solution pH was below the pH$_{zpc}$, the positive charges on MIL-68(In)-NH$_2$/GrO would repel AMX in positively charged forms. Similarly, in basic media, electrostatic repulsion would also generate between the same negatively charged AMX and MIL-68(In)-NH$_2$/GrO. However, at pH 5 the surface of the MIL-68(In)-NH$_2$/GrO composite with negative charges can be expected

Fig. 6. (a) PL spectra and (b) electrochemical impedance spectra of MIL-68(In)-NH$_2$ and MIL-68(In)-NH$_2$/GrO. Mott-Schottky plots of (c) MIL-68(In)-NH$_2$ and (d) MIL-68(In)-NH$_2$/GrO at different frequency.

Fig. 7. (a) Photocatalytic performance for aqueous AMX under different conditions (pH = 5). (b) TOC removal efficiency of MIL-68(In)-NH$_2$ and MIL-68(In)-NH$_2$/GrO (pH = 5). (c) Photodegradation efficiency of GrO, GrO+MIL-68(In)-NH$_2$, MIL-68(In)-NH$_2$ and MIL-68(In)-NH$_2$/GrO. (d) Photocatalytic activity of MIL-68(In)-NH$_2$/GrO for the degradation of AMX at different pH values.
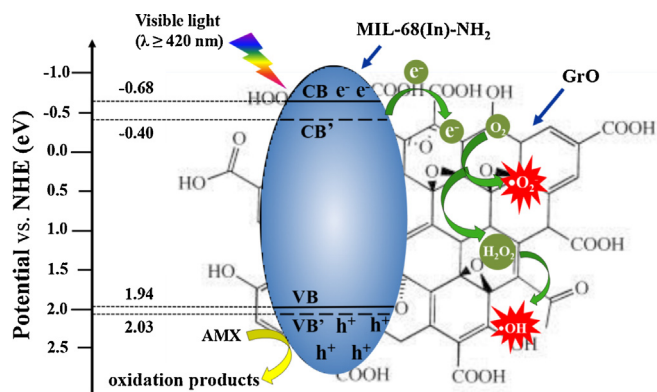
Fig. 8. Schematic diagram of the enhanced photocatalytic mechanism over the MIL-68(In)-NH$_2$/GrO composite.

Fig. 9. Reactive specie trapping experiments of MIL-68(In)-NH$_2$/GrO (pH = 5).

to provide high adsorption capability for the positively charged AMX, which should be responsible for the better photocatalytic performance toward AMX. In addition, it can be also observed that the photocatalytic activity at pH 6 was lower than at pH 5. The reason may be due to that AMX may mainly exist in the form of zwitterion at pH 6, which led to the ineffective adsorption of AMX on the MIL-68(In)-NH$_2$/GrO and thus the photocatalytic performance decreased. From the above results, it can be seen that the photocatalytic activity can be affected by the adsorption capacity of the photocatalyst toward the target pollutants. More importantly, it can be concluded that the solution pH had significant influence on the photodegradation of AMX by MIL-68(In)-NH$_2$/GrO.

Furthermore, the reusability and stability of the MIL-68(In)-NH$_2$/GrO composite for photocatalytic degradation of aqueous AMX were also investigated. The MIL-68(In)-NH$_2$/GrO sample was simply recovered by filtration, washed with pure water 3 times, and then dried in vacuum at 100 °C for 3 h. As shown in Fig. S5, a high AMX degradation efficiency was still achieved after three times of reuse. The XRD and FTIR analysis (Fig. S6) revealed that the MIL-68(In)-NH$_2$/GrO structure remained unchanged even after three consecutive cycles. These results sufficiently demonstrated the good reusability and stability of MIL-68(In)-NH$_2$/GrO and showed its potential in practical application.

3.3. Enhancement mechanism of photocatalytic activity

Based on the above experimental results, the enhanced photocatalytic mechanism of the MIL-68(In)-NH$_2$/GrO composite is proposed in Fig. 8. The indium-oxygen clusters within the substrate MOF of MIL-68(In)-NH$_2$/GrO can behave as quantum dots surrounded by terephthalate ligands. These organic bridging ligands can serve as antennas to harvest visible light and then effectively transfer the energy to the inorganic indium-oxygen clusters part. Subsequently, the photogenerated electrons on the CB of MIL-68(In)-NH$_2$ rapidly migrate to the GrO support, resulting in efficient carrier separation and thus an enhanced photocatalytic activity. Furthermore, more positive valance band potential for the MIL-68(In)-NH$_2$/GrO composite was obtained after GrO modification, which could provide higher photocatalytic oxidation ability of MIL-68(In)-NH$_2$/GrO toward the degradation of AMX. The E_{CB} and E_{VB} of MIL-68(In)-NH$_2$/GrO were calculated at -0.40 and 2.03 eV vs. NHE, respectively. The E_{CB} of MIL-68(In)-NH$_2$/GrO (-0.40 eV) is more negative than the O$_2$/•O$_2^-$ potential (-0.046 eV vs. NHE) and hence the photogenerated electrons on the CB of MIL-68(In)-NH$_2$ are favourable to reduce the O$_2$ [60]. Similarly, these electrons can also reduce O$_2$ to H$_2$O$_2$ (O$_2$/H$_2$O$_2$ is 0.915 eV vs. NHE) and the formed H$_2$O$_2$ would further transformed into •OH by capturing an electron [61]. Simultaneously, the photogenerated holes on the
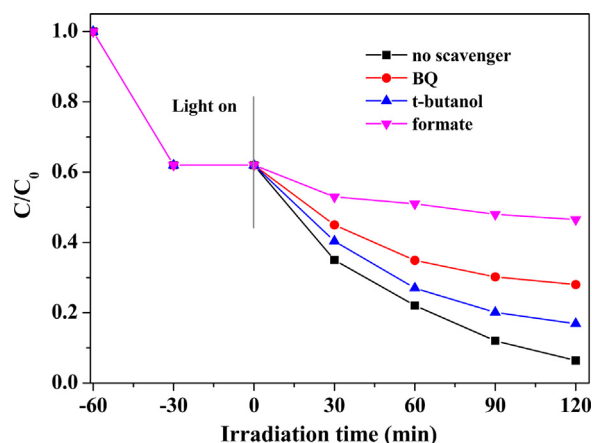
VB of MIL-68(In)-NH$_2$/GrO can directly oxidize the AMX, but not the OH$^-$ to yield •OH because of the lower positive potential of VB of MIL-68(In)-NH$_2$/GrO (2.03 eV) against the standard •OH/OH$^-$ (2.38 eV vs. NHE) [62]. To further investigate the roles of the reactive species (•O$_2^-$, •OH and h$^+$) in the photocatalytic process, 0.2 mM of BQ, t-butanol and formate were added as scavenging species of •O$_2^-$, •OH and h$^+$, respectively. As seen in Fig. 9, the photocatalytic degradation of AMX was inhibited in the order of formate > BQ > t-butanol. Consequently, h$^+$ and •O$_2^-$ played a dominant role for the AMX degradation in the MIL-68(In)-NH$_2$/GrO system.

4. Conclusions

In summary, the visible-light-driven photocatalytic degradation of AMX is for the first time realized over the MIL-68(In)-NH$_2$/GrO composite photocatalyst synthesized via a simple solvothermal method. The introduction of GrO resulted in improved visible light utilization, superior electron transport property as well as relatively high valence band potential and surface area, which then led to the enhanced photocatalytic activity of the MIL-68(In)-NH$_2$/GrO composite. Moreover, the photocatalytic performance of MIL-68(In)-NH$_2$/GrO was significantly affected by the solution pH, which was closely related to the adsorption of AMX on the photocatalyst. Furthermore, the MIL-68(In)-NH$_2$/GrO composite showed good reusability and stability. This work effectively confirms that the modification by using GrO (electron acceptor) was an effective way to promote photocatalytic activity, and it also provides important inspirations in developing other GrO-based composite photocatalysts and expanding the applications of MOFs.

Acknowledgment

Appendix A. Supplementary data

Supplementary data associated with this article can be found, in the online version, at http://dx.doi.org/10.1016/j.apcatb.2016.07.057.

References

[1] Q.Q. Zhang, G.G. Ying, C.G. Pan, Y.S. Liu, J.L. Zhao, Environ. Sci. Technol. 49 (2015) 6772–6782.
[2] T.B. Minh, H.W. Leung, I.H. Loi, W.H. Chan, M.K. So, J.Q. Mao, D. Choi, J.C. Lam, G. Zheng, M. Martin, Mar. Pollut. Bull. 58 (2009) 1052–1062.

[3] M.A.F. Locatelli, F.F. Sodré, W.F. Jardim, Arch. Environ. Contam. Toxicol. 60 (2011) 385–393.

[4] A. Watkinson, E. Murby, D. Kolpin, S. Costanzo, Sci. Total Environ. 407 (2009) 2711–2723.

[5] L. Rizzo, C. Manaia, C. Merlin, T. Schwartz, C. Dagot, M. Ploy, I. Michael, D. Fatta-Kassinos, Sci. Total Environ. 447 (2013) 345–360.

[6] A. Pérez-Parada, A. Agüera, M.d.M. Gómez-Ramos, J.F. García-Reyes, H. Heinzen, A.R. Fernández-Alba, Rapid Commun. Mass Spectrom. 25 (2011) 731–742.

[7] M. del Mar Gómez-Ramos, A. Pérez-Parada, J.F. García-Reyes, A.R. Fernández-Alba, A. Agüera, J. Chromatogr. A 1218 (2011) 8002–8012.

[8] Y. Zhang, C.F. Marrs, C. Simon, C. Xi, Sci. Total Environ. 407 (2009) 3702–3706.

[9] A. Schlüter, R. Szczepanowski, A. Pühler, E.M. Top, FEMS Microbiol. Rev. 31 (2007) 449–477.

[10] S. Zha, Y. Cheng, Y. Gao, Z. Chen, M. Megharaj, R. Naidu, Chem. Eng. J. 255 (2014) 141–148.

[11] J.H.O.S. Pereira, A.C. Reis, V. Homem, J.A. Silva, A. Alves, M.T. Borges, R.A.R. Boaventura, V.J.P. Vilar, O.C. Nunes, Water Res. 65 (2014) 307–320.

[12] A.G. Trovo, R.F. Nogueira, A. Aguera, A.R. Fernandez-Alba, S. Malato, Water Res. 45 (2011) 1394–1402.

[13] N.F.F. Moreira, C.A. Orge, A.R. Ribeiro, J.L. Faria, O.C. Nunes, M.F.R. Pereira, A.M.T. Silva, Water Res. 87 (2015) 87–96.

[14] M. Pourakbar, G. Moussavi, S. Shekoohiyan, Ecotoxicol. Environ. Saf. 125 (2016) 72–77.

[15] D. Klauson, J. Babkina, K. Stepanova, M. Krichevskaya, S. Preis, Catal. Today 151 (2010) 39–45.

[16] D. Dimitrakopoulou, I. Rethemiotaki, Z. Frontistis, N.P. Xekoukoulotakis, D. Venieri, D. Mantzavinos, J. Environ. Manag. 98 (2012) 168–174.

[17] D. Kanakaraju, J. Kockler, C.A. Motti, B.D. Glass, M. Oelgemöller, Appl. Catal. B 166–167 (2015) 45–55.

[18] K.H. Leong, S.L. Liu, L.C. Sim, P. Saravanan, M. Jang, S. Ibrahim, Appl. Surf. Sci. 358 (2015) 370–376.

[19] E.S. Elmolla, M. Chaudhuri, Desalination 252 (2010) 46–52.

[20] E.S. Elmolla, M. Chaudhuri, J. Hazard. Mater. 173 (2010) 445–449.

[21] M. Alvaro, E. Carbonell, B. Ferrer, F.X. Llabrés i Xamena, H. Garcia, Chem. Eur. J. 13 (2007) 5106–5112.

[22] Y. Xu, M. Lv, H. Yang, Q. Chen, X. Liu, F. Wei, RSC Adv. (2015).

[23] L. Shi, T. Wang, H. Zhang, K. Chang, J. Ye, Adv. Funct. Mater. 25 (2015) 5360–5367.

[24] J. He, Z. Yan, J. Wang, J. Xie, L. Jiang, Y. Shi, F. Yuan, F. Yu, Y. Sun, Chem. Commun. (Camb) 49 (2013) 6761–6763.

[25] M. Savonnet, D. Bazer-Bachi, C. Pinel, V. Lecocq, N. Bats, D. Farrusseng, FR Patent (2009) 09/05.101.

[26] L. Wu, M. Xue, S.L. Qiu, G. Chaplais, A. Simon-Masseron, J. Patarin, Microporous Mesoporous Mat. 157 (2012) 75–81.

[27] R. Liang, L. Shen, F. Jing, W. Wu, N. Qin, R. Lin, L. Wu, Appl. Catal. B 162 (2015) 245–251.

[28] L. Shen, S. Liang, W. Wu, R. Liang, L. Wu, J. Mater. Chem. A 1 (2013) 11473.

[29] J. Di, J. Xia, Y. Ge, H. Li, H. Ji, H. Xu, Q. Zhang, H. Li, M. Li, Appl. Catal. B 168–169 (2015) 51–61.

[30] C. Liu, L. Wang, Y. Tang, S. Luo, Y. Liu, S. Zhang, Y. Zeng, Y. Xu, Appl. Catal. B 164 (2015) 1–9.

[31] H. Wang, X. Yuan, Y. Wu, H. Huang, X. Peng, G. Zeng, H. Zhong, J. Liang, M. Ren, Adv. Colloid Interface Sci. 195 (2013) 19–40.

[32] X.J. Chen, Y.Z. Dai, X.Y. Wang, J. Guo, T.H. Liu, F.F. Li, J. Hazard. Mater. 292 (2015) 9–18.

[33] K. Dai, L. Lu, C. Liang, G. Zhu, Q. Liu, L. Geng, J. He, Dalton Trans. 44 (2015) 7903–7910.

[34] X.F. Shi, X.Y. Xia, G.W. Cui, N. Deng, Y.Q. Zhao, L.H. Zhuo, B. Tang, Appl. Catal. B 163 (2015) 123–128.

[35] M. Zhu, P. Chen, M. Liu, Acs Nano 5 (2011) 4529–4536.

[36] C. Petit, T.J. Bandosz, Adv. Funct. Mater. 21 (2011) 2108–2117.

[37] D. Xu, B. Cheng, S. Cao, J. Yu, Appl. Catal. B 164 (2015) 380–388.

[38] L. Liu, J. Liu, D.D. Sun, Catal. Sci. Technol. 2 (2012) 2525.

[39] P. Lian, X. Zhu, S. Liang, Z. Li, W. Yang, H. Wang, Electrochim. Acta 55 (2010) 3909–3914.

[40] C. Petit, J. Burress, T.J. Bandosz, Carbon 49 (2011) 563–572.

[41] X. Zhou, W. Huang, J. Shi, Z. Zhao, Q. Xia, Y. Li, H. Wang, Z. Li, J. Mater. Chem. A 2 (2014) 4722.

[42] K.N. Kudin, B. Ozbas, H.C. Schniepp, R.K. Prud'Homme, I.A. Aksay, R. Car, Nano Lett. 8 (2008) 36–41.

[43] Y. Xu, H. Bai, G. Lu, C. Li, G. Shi, J. Am. Chem. Soc. 130 (2008) 5856–5857.

[44] H.L. Guo, X.F. Wang, Q.Y. Qian, F.B. Wang, X.H. Xia, ACS Nano 3 (2009) 2653–2659.

[45] M. Seredych, C. Petit, A.V. Tamashausky, T.J. Bandosz, Carbon 47 (2009) 445–456.

[46] J. Rouquerol, F. Rouquerol, K.S.W. Sing, Academic Press : San Diego, 1 (1999) 99.

[47] M. Samadi, H.A. Shivaee, M. Zanetti, A. Pourjavadi, A. Moshfegh, J. Mol. Catal. A: Chem. 359 (2012) 42–48.

[48] W. Zhou, T. Xiong, C. Shi, J. Zhou, K. Zhou, N. Zhu, L. Li, Z. Tang, S. Chen, Angew. Chem. 55 (2016) 8416–8420.

[49] T. Peng, K. Li, P. Zeng, Q. Zhang, X. Zhang, J. Phys. Chem. C 116 (2012) 22720–22726.

[50] D. Xu, B. Cheng, S. Cao, J. Yu, Appl. Catal. B 164 (2015) 380–388.

[51] T. Peng, K. Li, P. Zeng, Q. Zhang, X. Zhang, J. Phys. Chem. C 116 (2012) 22720–22726.

[52] V. Spagnol, E. Sutter, C. Debiemme-Chouvy, H. Cachet, B. Baroux, Electrochim. Acta 54 (2009) 1228–1232.

[53] D.S. Kong, Langmuir 24 (2008) 5324–5331.

[54] A. Ishikawa, T. Takata, J.N. Kondo, M. Hara, H. Kobayashi, K. Domen, J. Am. Chem. Soc. 124 (2002) 13547–13553.

[55] H. Zia, N. Shalchian, F. Borhanian, Can. J. Pharm. Sci. 12 (1977) 80–83.

[56] R. Andreozzi, M. Canterino, R. Marotta, N. Paxeus, J. Hazard. Mater. 122 (2005) 243–250.

[57] V. Chemie, Germany : Duisburg University, (2005).

[58] A.G. Trovó, R.F.P. Nogueira, A. Agüera, A.R. Fernandez-Alba, S. Malato, Water Res. 45 (2011) 1394–1402.

[59] D. Kanakaraju, J. Kockler, C.A. Motti, B.D. Glass, M. Oelgemöller, Appl. Catal. B 166 (2015) 45–55.

[60] L. Ye, J. Chen, L. Tian, J. Liu, T. Peng, K. Deng, L. Zan, Appl. Catal. B 130–131 (2013) 1–7.

[61] F. Dong, Q. Li, Y. Sun, W.K. Ho, ACS Catal. 4 (2014) 4341–4350.

[62] H. Cheng, B. Huang, Y. Dai, X. Qin, X. Zhang, Langmuir 26 (2010) 6618–6624.